Coexistence of low-frequency spin-torque ferromagnetic resonance and unidirectional spin Hall magnetoresistance

Motomi Aoki, Ei Shigematsu, Ryo Ohshima, Teruya Shinjo, Masashi Shiraishi, and Yuichiro Ando

Phys. Rev. B **104**, 094401 — Published 1 September 2021

DOI: 10.1103/PhysRevB.104.094401

Coexistence of low-frequency spin-torque ferromagnetic resonance and unidirectional spin Hall magnetoresistance

Motomi Aoki[1], Ei Shigematsu[1], Ryo Ohshima[1], Teruya Shinjo[1], Masashi Shiraishi[1], and Yuichiro Ando[1,2†]

[1]Department of Electronic Science and Engineering, Kyoto University, Kyoto, Kyoto 615-8510, Japan

[2]PRESTO, Japan Science and Technology Agency, Honcho, Kawaguchi, Saitama 332-0012, Japan

Corresponding authors

[†]**Yuichiro Ando** Address: A1-226, Kyodai Katsura, Nishikyo-ku, Kyoto, Kyoto, Japan

Tel.: +81-75-383-2356, Fax: +81-75-383-2275

E-mail: ando.yuichiro.5s@kyoto-u.ac.jp

Abstract

We investigate the DC voltage under an applied microwave current for platinum(Pt)/cobalt(Co), tantalum(Ta)/Co, and tungsten(W)/Co bilayers, where the microwave-induced alternating magnetic field (B_{rf}) is parallel to an external static magnetic field (B_{ext}). Whereas spin torque ferromagnetic resonance (ST-FMR) signals do not appear because of the parallel configuration of B_{rf} and the magnetization of the Co layer, we recently found a clear hysteresis signal around B_{ext} = 0 mT only when the microwave frequency (f_{MW}) is low, typically less than 10 GHz. This low-frequency ST-FMR (LFST-FMR) signal enables us to detect magnetization switching induced by spin-orbit torque (SOT) with high sensitivity. In this study, we found an additional background (BG) signal superimposed on the LSFT-FMR signal. The additional BG signal also has hysteresis behavior and appears even at high f_{MW}, where the LSFT-FMR signal completely disappears. The sign of the BG signal is changed by changing the nonmagnetic material from Pt to Ta or W. By measuring f_{MW}, the microwave current, the temperature, and the magnetic-field-angle dependences, we conclude that the BG signal is induced by spin-dependent unidirectional spin Hall magnetoresistance (SD-USMR), which is generated by a spin current induced by the spin Hall effect of nonmagnetic metals and spin-dependent electron mobility in ferromagnetic metals. The SD-USMR signal appears in wide ranges of f_{MW} and B_{ext} because the SD-USMR originates from the nonlinearity of current-dependent resistance and is not related to magnetization dynamics. From the magnitude of the BG signal, the spin Hall angles of Pt and Ta are calculated to be 0.026±0.006 and –0.042±0.006, respectively. In addition, we demonstrate SOT magnetization switching using the BG signal.

□. INTRODUCTION

Spin-orbit torque (SOT) is one of the most attractive research areas of spintronics [1,2] because it enables low-power consumption and highly enduring magnetization switching in magnetoresistive random access memory (MRAM). A material with a large spin Hall angle, θ_{SH}, is essential for efficient writing of MRAM using SOT. Therefore, many researchers have experimentally investigated θ_{SH} for various materials [3–13]. Spin torque ferromagnetic resonance (ST-FMR) is one of the most widely used methods for evaluating θ_{SH} [14]. In this method, an alternating current, I_{rf}, for generation of microwaves is injected into a nonmagnetic metal (NM)/ ferromagnetic metal (FM) bilayer under an applied static magnetic field, B_{ext}. A microwave alternating magnetic field, B_{rf}, and/or SOT generated by the spin Hall effect (SHE) in the NM layer induces precession of the magnetization of the FM layer. The magnetization precession is converted into an oscillation of the resistance of the NM/FM bilayer, $R_{NM/FM}$, via the anisotropic magnetoresistance (AMR) of the FM layer. The oscillating $R_{NM/FM}$ and I_{rf} generate a DC voltage, V_{DC}, whose amplitude is maximized around the ferromagnetic resonance (FMR) condition. θ_{SH} is estimated by analyzing the V_{DC}–B_{ext} spectra. Note that the ST-FMR does not generally appear when a sufficiently large B_{ext} is applied perpendicular to the direction of I_{rf} because neither B_{rf} nor the SOT induces a torque on the magnetization. On the contrary, recently we found that a strong DC voltage is also generated even when B_{ext} is perpendicular to the direction of I_{rf}, especially when the microwave frequency, f_{MW}, is less than 10 GHz. This is called low-frequency ST-FMR (LFST-FMR) [15]. The LFST-FMR generally appear at low B_{ext}. The origin of the LFST-FMR is the finite slope in a $R_{NM/FM}$–B_{ext} curve around B_{ext} = 0 mT [16]. Because the magnetic domain structure is not uniform around B_{ext} = 0 mT, particularly at the edge of the FM layer owing to the shape anisotropy, the total magnetization of whole FM layer at positive I_{rf} is different from that at negative I_{rf}. This results in oscillation of $R_{NM/FM}$ and generation of V_{DC}.

LFST-FMR is expected to accelerate investigations of SOT materials because it enables highly sensitive detection of SOT-induced magnetization switching of the FM layer with in-plane magnetic anisotropy without complicated device fabrication. Actually, magnetization switching of 100 nm-wide ferromagnetic electrodes was successfully demonstrated owing to the high sensitivity. However, the origin of LFST-FMR has not been completely revealed. The obtained LFST-FMR spectrum was approximately a factor of two larger than the one calculated in our previous research [15]. Although the magnitude of the LFST-FMR was shown to depend on the slope of the $R_{NM/FM}$–B_{ext} curve, it still deviated from the calculation [17]. Therefore, a contribution to the LFST-FMR spectrum other than from the $R_{NM/FM}$–B_{ext} slope is expected.

In this study, we found an additional background (BG) signal superimposed on the LFST-FMR spectra and even

on the ST-FMR spectra. We concluded that this BG signal is generated by the unidirectional spin Hall magnetoresistance (USMR) caused by the SHE in the NM layer [18–23]. In the USMR, the spin-dependent interfacial and/or bulk resistance of the FM layer and spin-dependent electron mobility play an important role in generating V_{DC}. In an NM/FM bilayer with a finite spin–orbit coupling of the NM layer, a spin current generated by the SHE in the NM layer is injected into the FM layer. The spin polarization of this spin current is reversed depending on the polarity of I_{rf}. In this situation, the total resistance also has a nonlinear I_{rf} dependence, resulting in generation of V_{DC}. By measuring f_{MW}, the amplitude of I_{rf}, the temperature, and magnetic field angle dependences of the BG signal, we concluded that the origin of the BG signal is the spin-dependent USMR (SD-USMR) [22]. The magnitude of the SD-USMR has been theoretically investigated and calculated using the spin diffusion equation [20]. From the magnitude of the BG signal, we estimated θ_{SH} for Pt and Ta to be 0.026±0.006 and –0.042±0.006, respectively. We also detected SOT magnetization switching using the hysteresis characteristics of the BG signal. Because the SD-USMR is induced by the spin-dependent conductivity of the FM and is not related to spin torque or magnetization dynamics, we successfully detected magnetization switching even when f_{MW} was high at 13 GHz. The threshold current density was 3×10^7 A/cm^2, which is consistent with a previous research (1.8×10^7 A/cm^2) [24]. Under a specific condition, we can enhance V_{DC} using both the LFST-FMR and the SD-USMR, which enables more efficient detection of the magnetization switching. The SD-USMR is also superimposed on the ST-FMR signals because it appears universally irrespective of f_{MW}, magnetic field angle, and device geometry. Once the parameters such as spin diffusion length, polarization of the electron mobility, and the anomalous Nernst voltage are obtained by additional experiments, this allows us to estimate θ_{SH} from two different perspectives, i.e., spin torque and spin dependent magnetoresistance, by only measuring one FMR spectrum, which enables the cross check and more reliable evaluation of θ_{SH}.

□. SAMPLE FABRICATION AND EXPERIMENTAL PROCEDURE

Figure 1(a) shows a schematic of the device structure and electric circuit in this study. First, rectangular NM(t_N)/Co(t_F)/SiO$_2$(t_{cap}) layers were fabricated via electron beam lithography and rf magnetron sputtering. The quantities t_N, t_F, and t_{cap} are the thicknesses of the NM, Co, and SiO$_2$ layers in nanometers (nm), respectively. Then, a rectangular ferromagnetic Co/SiO$_2$ region with width w and length l was fabricated using electron beam lithography and argon ion (Ar^+) milling. The Ar^+ milling was stopped after etching of a ~2 nm NM layer to make the lead line of the remaining NM later. After an additional Ar^+ milling to remove the surface oxidized layer of the NM lead line, a Ti (3 nm)/Au (70 nm) electrode was deposited via electron beam deposition without breaking

vacuum. We prepared several NM(t_N)/Co(t_F)/SiO_2(t_{cap}) samples with various geometries and materials as follows: Pt(15)/Co(3)/SiO_2(7) (sample A, w = 5 μm, l = 0.8 μm), Pt(15)/Co(3)/SiO_2(7) (sample B, w = 40 μm, l = 40 μm), Ta(15)/Co(3)/SiO_2(7) (sample C, w = 5 μm, l = 1 μm), Ta(15)/Co(8)/SiO_2(7) (sample D, w = 10 μm, l = 1.3 μm), Ta(15)/Co(3)/SiO_2(7) (sample E, w = 40 μm, l = 40 μm), and W(6)/Co(1)/SiO_2(3) (sample F, w = 5 μm, l = 5 μm), as summarized in Table 1. Microwave radiation with a power P_{MW} was applied via an analog commercial signal generator (KEYSIGHT N5173B EXG). V_{DC} was measured using a voltmeter (Keithley Nanovoltmeter 2182A). To demonstrate SOT magnetization switching, a 1-μs-wide pulse current was injected using a function generator (KEYSHIGHT 33622A) to switch the magnetization. We used a physical property measurement system (Quantum Design: PPMS) to measure the V_{DC}–B_{ext} curves at low temperature. V_{DC} was measured using a voltmeter (Keithley Nanovoltmeter 2182A) under microwave irradiation generated by a function generator (KEYSHIGHT 33622A) with a frequency of 0.1 GHz. The amplitude of the voltage for generating I_{rf}, V_{MW}, was fixed to 2 V peak-to-peak. B_{ext} was applied along the y axis as shown in Fig. 1(a). The experiments were carried out at room temperature unless otherwise indicated.

□. RECTIFICATION SIGNAL UNDER MICROWAVE IRRADIATION

When f_{MW} is lower than the ferromagnetic resonance (FMR) frequency, a non-zero V_{DC} is generated around B_{ext} = 0 mT via the oscillation of $R_{NM/FM}$ due to the LFST-FMR [15]. V_{DC} generated by the LFST-FMR, V_{LF}, is expressed as

$$V_{\mathrm{LF}} = \frac{1}{2} I_{\mathrm{rf}}^{0} B_{\mathrm{eff}}^{0} \frac{\Delta R_{\mathrm{NM/FM}}}{\Delta B_{\mathrm{ext}}}, \tag{1}$$

where definitions of I_{rf}^{0} and B_{eff}^{0} are $I_{\mathrm{rf}} = I_{\mathrm{rf}}^{0} \sin 2\pi f_{\mathrm{MW}} t$ and $B_{\mathrm{eff}} = B_{\mathrm{eff}}^{0} \sin 2\pi f_{\mathrm{MW}} t$, respectively. B_{eff} is composed of B_{rf} induced by the part of I_{rf} flowing through the NM layer and the spin Hall effective field, B_{SH}, corresponding to the field-like spin orbit torque. ΔB_{ext} is the peak-to-peak value of B_{rf}+B_{SH}, and $|B_{rf}|>|B_{SH}|$ was confirmed in this study. Considering that the signs of I_{rf} and B_{rf} are always opposite in our device structure, V_{LF} is proportional to $-\frac{\Delta R_{\mathrm{NM/FM}}}{\Delta B_{\mathrm{ext}}}$. The contribution of damping-like SOT is negligible for generating V_{LF}, because the phase difference between the oscillating magnetization and I_{rf} is almost 0° when f_{MW} is sufficiently low compared with that for the FMR conditions. Figures 1(b)–1(d) show the B_{ext} dependences of (b) $R_{NM/FM}$, which was obtained by monitoring DC voltage with an application of a DC charge current; (c) $-\frac{\Delta R_{\mathrm{NM/FM}}}{\Delta B_{\mathrm{ext}}}$; and (d) the rectification voltage under microwave, V_{DC}, for sample A. Here, ΔB_{ext} was set to 0.2 mT. The shape of the V_{DC}–B_{ext} curve in Fig.

1(d) roughly corresponds to that of the $-\frac{\Delta R_{\mathrm{NM/FM}}}{\Delta B_{\mathrm{ext}}}$ – B_{ext} curve in Fig. 1(c). Note that the signal shape of $-\frac{\Delta R_{\mathrm{NM/FM}}}{\Delta B_{\mathrm{ext}}}$ – B_{ext} curve were almost unchanged even though different ΔB_{ext} i.e., different B_{SH} was employed. [see the Supplemental material, SM, A [25]] Figures 1(e)–1(g) show the B_{ext} dependences of (e) $R_{\mathrm{NM/FM}}$; (f) $-\frac{\Delta R_{\mathrm{NM/FM}}}{\Delta B_{\mathrm{ext}}}$; and (g) V_{DC} for sample C. In contrast to sample A, there are clear differences between the $-\frac{\Delta R_{\mathrm{NM/FM}}}{\Delta B_{\mathrm{ext}}}$ – B_{ext} and V_{DC}–B_{ext} curves as shown in Figs. 1(f) and 1(g). For example, V_{DC} at strong positive B_{ext} is clearly lower than at strong negative B_{ext}, indicating an additional background voltage. We can recognize the LFST-FMR with switching fields at ±20 mT as indicated by the blue arrows, which correspond to the switching fields in Fig. 1(f). It seems that a BG signal with an odd function and a saturation around $|B_{\mathrm{ext}}| \geq 30$ mT is superimposed on the LFST-FMR. The magnitude of the BG signal, V_{BG}, is defined as $2V_{\mathrm{BG}} = V_{\mathrm{DC}}^{+} - V_{\mathrm{DC}}^{-}$, where V_{DC}^{+} (V_{DC}^{-}) is the average of V_{DC} at B_{ext} > 50 mT (B_{ext} < −50 mT). Note that the ST-FMR was negligible in our measurement setup because B_{ext} was applied perpendicular to the direction of I_{rf}. Whereas relatively low V_{BG} is also recognized for sample A, its sign is opposite to that of sample C. Therefore, V_{BG} might have a relationship with θ_{SH} because the signs of θ_{SH} for Pt and Ta are opposite to each other. One possible origin of the BG signal is a thermoelectric effect such as the anomalous Nernst effect (ANE) [26,27] and the spin-dependent Seebeck effect (SDSE) [28–30]. Owing to the non-uniform flow of I_{rf} in the NM/FM bilayers and unequal heat conductivity between the top and bottom surfaces, a thermal gradient perpendicular to the film plane is expected to be generated [8,31]. This thermal gradient generates an electromotive force along the *x* direction in Fig. 1(a) whose sign depends on the magnetization direction. However, the ANE, which is dominant over the SDSE in the NM/Co bilayers, shows the same sign irrespective of θ_{SH} for the adjacent NM [31–34] because the direction of thermal gradient in the Co layer of the Pt/Co and the Ta/Co samples are the same due to the large heat conductance of the MgO substrate [see SM-B and SM-C]. Therefore, whereas a non-negligible contribution by the ANE might exist, it is not the dominant origin of the BG signal.

IV. FREQUENCY DEPENDENCE

In this section, we investigate the large BG signal observed in the Ta/Co bilayer at various f_{MW} values. Figure 2(a) shows V_{DC}–B_{ext} curves under various f_{MW} values for sample C. Figure 2(b) shows the enlarged signal of the meshed area (from –40 to +40 mT) in Fig. 2(a). For f_{MW} > 5 GHz, a simple hysteresis is observed where V_{DC} for the up sweep is higher than for the down sweep at B_{ext} = 0 mT. In contrast, for f_{MW} < 3 GHz, the hysteresis signals cross at $|B_{\mathrm{ext}}| \leq 5$ mT; i.e., V_{DC} for the up sweep becomes lower than for the down sweep. The magnitude of the LFST-

FMR has a strong f_{MW} dependence and becomes almost zero at high f_{MW}. Because of this, the crossing of the hysteresis signals at $f_{MW} < 3$ GHz is due to the appearance of the LFST-FMR where V_{DC} for the up sweep is expected to be lower than for the down sweep at $B_{ext} = 0$ mT, as shown in Fig. 1(f). Since the LFST-FMR disappears at high f_{MW}, we found that the BG signal also shows hysteresis and appears even at higher f_{MW} for $f_{MW} > 5$ GHz. Figures 2(c) and 2(d) respectively show the V_{DC}–B_{ext} curves under various f_{MW} values and enlarged plots for sample D, which had a thicker Co layer. In this case, the LFST-FMR became dominant for $f_{MW} < 3$ GHz, whereas the BG signals became dominant for $f_{MW} > 7$ GHz. At $f_{MW} = 5$ GHz, these signals canceled each other out. The magnetoresistance of the Co/Ta bilayer induced by the AMR of the Co layer increases with increasing t_F owing to the increased contribution of the conductance of the Co layer. This enhances the LFST-FMR originating from AMR for sample D. The difference in behaviors between samples C and D in Fig. 2 indicates that the origin of the BG signals is not directly related to AMR. Additionally, V_{DC} in the V_{DC}–B_{ext} curves becomes constant at strong negative or positive B_{ext} in Fig. 2. This indicates that the BG signals do not originate from magnetization dynamics, because the magnetization is completely aligned along the $-y$ or $+y$ direction owing to strong B_{ext} and does not change even under microwave irradiation.

V. DC VOLTAGE INDUCED BY UNIDIRECTIONAL SPIN HALL MAGNETORESISTANCE

The BG signal is not related to the temperature gradient, AMR, or magnetization dynamics. Therefore, we focus on the USMR [18–23], where the in-plane resistance perpendicular to the magnetization in an NM/FM structure depends on the polarity of the charge current. There are two USMR mechanisms. One is the spin-dependent USMR (SD-USMR) [22], the origin of which is the spin-dependent resistance at the NM/FM interface and/or in the FM layer caused by a spin current generated via the SHE of the NM layer. In this case, the spin-dependent electron mobility generates a nonlinear magnetoresistance. The other mechanism is the spin-flip USMR (SF-USMR) [22], where modulation of the magnon population due to spin injection via the SHE in the NM layer causes modulation of the electron–magnon scattering at the NM/FM interface. Typically, the magnitude of the SF-USMR is suppressed at strong B_{ext} [23], which is inconsistent with the behavior obtained in Fig. 2. Therefore, the most likely origin of the BG signals is the SD-USMR. From a simple spin diffusion model, the magnetoresistance induced by the SD-USMR, $MR_{SD\text{-}USMR}$, with spin-dependent electron mobility is expressed as [20]

$$MR_{\mathrm{SD-USMR}} = 6\left(\frac{\sigma_{\mathrm{F}}L_{\mathrm{F}}}{\sigma_{\mathrm{N}}t_{\mathrm{N}}+\sigma_{\mathrm{F}}t_{\mathrm{F}}}\right)\frac{(p_\sigma - p_{\mathrm{N}})\left(\left(\frac{\theta_{\mathrm{SH}}L_{\mathrm{N}}}{\varepsilon_{\mathrm{F}}}\right)\tanh\left(\frac{t_{\mathrm{N}}}{2L_{\mathrm{N}}}\right)\tanh\left(\frac{t_{\mathrm{F}}}{L_{\mathrm{F}}}\right)\right)}{1+(1-p_\sigma^2)\left(\frac{\sigma_{\mathrm{F}}L_{\mathrm{N}}}{\sigma_{\mathrm{N}}L_{\mathrm{F}}}\right)\tanh\left(\frac{t_{\mathrm{F}}}{L_{\mathrm{F}}}\right)\coth\left(\frac{t_{\mathrm{N}}}{L_{\mathrm{N}}}\right)}\frac{IR_{\mathrm{NM/FM}}}{l}, \quad (2)$$

where I, $\sigma_{F(N)}$, and $L_{F(N)}$ are the longitudinal current, the bulk conductivity, and the spin diffusion length of the FM (NM), respectively; p_σ is the conductivity spin asymmetry induced by the spin-dependent electron mobility; p_N is the difference in density of states at the Fermi energy between the up and down spins; and ε_F is the Fermi energy of the FM. When I_{rf} is applied, the time average of the voltage induced by the SD-USMR, V_{BG}, is expressed as

$$V_{BG} = \frac{R_{NM/FM}^2}{l} 3\left(\frac{\sigma_F L_F}{\sigma_N t_N + \sigma_F t_F}\right) \frac{(p_\sigma - p_N)\left(\left(\frac{\theta_{SH} L_N}{\varepsilon_F}\right)\tanh\left(\frac{t_N}{2L_N}\right)\tanh\left(\frac{t_F}{L_F}\right)\right)}{1 + (1 - p_\sigma^2)\left(\frac{\sigma_F L_N}{\sigma_N L_F}\right)\tanh\left(\frac{t_F}{L_F}\right)\coth\left(\frac{t_N}{L_N}\right)} {I_{rf}^0}^2. \quad (3)$$

Because the polarities of p_σ and p_N are changed by the magnetization reversal and their magnitudes are constant unless the magnetization direction changes, V_{BG} in Eq. (3) is consistent with the BG signals obtained in Fig. 2. Furthermore, the polarity of V_{BG} depends on θ_{SH}, which is consistent with the polarity change of V_{BG} between samples A and C. For the LFST-FMR, the DC voltage is generated by the product of the oscillating resistance due to magnetization precession and the AC current, which has the same frequency. This is the spin rectification effect. In contrast, for the SD-USMR, the DC voltage is generated by the charge current dependence on magnetoresistance. Therefore, it is not related to the magnetization dynamics and appears in wide ranges of f_{MW} and B_{ext}. The t_F dependence is also expected to be different because the magnitude of the SD-USMR is maximized at a specific value that is related to L_F.

VI. CURRENT, TEMPERATURE, AND ANGLE DEPENDENCES

To verify that the BG signal is actually generated by the SD-USMR, we measured V_{BG} under various conditions. Figure 3(a) shows $V_{BG}/{I_{rf}^0}^2$ as a function of f_{MW}. Taking into account the frequency-dependent attenuation in the measurement system because of impedance mismatch, I_{rf}^0 was estimated using a vector network analyzer (Agilent E5071C). No clear relationship was found between $V_{BG}/{I_{rf}^0}^2$ and f_{MW}, which is consistent with the characteristics of SD-USMR. Next, we investigated the I_{rf}^0 dependence of V_{BG} by changing P_{MW} from 0 to 13 dBm as shown in Fig. 3(b). V_{BG} was proportional to ${I_{rf}^0}^2$, in agreement with Eq. (3). The temperature dependence of V_{BG} was also investigated using PPMS for sample E. Figure 3(c) also shows the conjectured temperature evolution starting from 300 K of the DC voltage generated by the SF-USMR using values in Ref. [22]. The DC voltage generated by the SF-USMR approaches 0 V by decreasing the temperature because of suppression of magnon, obviously different from our results. Considering the measured temperature dependences in $\sigma_{F(N)}$ and expected temperature dependences in θ_{SH}, L_F, L_N, and the polarity of the magnetization in Co [35–37], the SD-USMR in Ta/Co is expected to have a smaller temperature dependence than the SF-USMR [21–23]. Note that the USMR induced by the high-

energy magnon might also contribute to V_{BG} because it is constant up to $B_{ext} \sim 5$ T [38]. However, the USMR induced by the high-energy magnon is suppressed in the low temperature, which is inconsistent with our experimental result. Therefore, the obtained temperature dependence of V_{BG} is consistent with that of the SD-USMR.

We also investigated V_{BG} under a strong external magnetic field ($B_{ext} = 2$ T) along different directions for sample E. Figures 4(a)–4(c) show the definitions of three different angles, α, β, and γ. Figure 4(d) shows the α, β, and γ dependences of V_{BG}. The solid lines are linear fits indicated by sin α and sin γ_M, where γ_M is the angle between the magnetization and the y axis calculated using micromagnetic simulation. As shown in Fig. 4(d), V_{BG} is proportional to sin α and sin γ_M (the y component of magnetization), which is also consistent with previous studies on SD-USMR [18,19,21,39]. Note that if the origin of V_{BG} is magnon-induced USMR, it should shows a different angular dependences [22]. Because the frequency, current, temperature, and magnetic-field-angle dependences of V_{BG} were consistent with those of the SD-USMR, we concluded that V_{BG} was mainly induced by the SD-USMR.

VII. DECONVOLUTION OF THE SIGNAL

Since the BG signal was mainly generated by the SD-USMR, the magnitude of which is proportional to the y component of the magnetization, we can differentiate the contribution from the BG signal and the LFST-FMR in all field range, respectively. y component of the magnetization direction was estimated from the AMR signal in the $R_{NM/FM}$-B_{ext} curve shown in Fig. 1(b) and 1(e). The calculated V_{DC}-B_{ext} curves due to the SD-USMR for sample A and sample C are shown in Figs. 5(a) and 5(b). Clear rectangular shape signals with small rotation around switching fields were obtained. Figures 5(c) and 5(d) show the difference between experimentally obtained V_{DC}-B_{ext} curves (Figs. 1(d) and 1(g)) and the calculated V_{DC}-B_{ext} curves due to the SD-USMR (Figs. 5(a) and 5(c)) for sample A and sample C, respectively. The signal shapes of Figs. 5(c) and 5(d) are both similar to those of $-\frac{\Delta R_{NM/FM}}{\Delta B_{ext}} - B_{ext}$ curves shown in Figs. 1(c) and 1(f), respectively, indicating dominant contribution of the LFST-FMR. We found that whereas the signal shapes of Figs. 5(c) and 5(d) are almost the same for samples A and C, those of Figs. 5(a) and 5(b) exhibit finite differences in polarity and magnitude. Whereas the magnitude of the signal in Fig. 5(c) is dominant for sample A, that in Fig. 5(d) is comparable to that in Fig. 5(b) for sample C.

VIII. DETERMINATION OF SPIN HALL ANGLE

We determined θ_{SH} for Pt and Ta from V_{BG} measured in samples B and E. To exclude the contribution from V_{LF}, we applied a strong B_{ext} up to 1 T using PPMS and redefined V_{DC}^{+} (V_{DC}^{-}) as the average of V_{DC} at $B_{ext} > 200$ mT ($B_{ext} < -200$ mT). V_{MW} and f_{MW} were set to 2 V peak-to-peak and 0.1 GHz, respectively. We measured V_{BG} as 67 ± 15 nV

and −460 ± 70 nV for samples B and E, respectively. Although we experimentally verified that V_{BG} is mainly generated from the SD-USMR, a non-negligible contribution from the ANE is also expected [18]. Therefore, we calculated the temperature gradient induced by Joule heating using COMSOL Multiphysics [40,41] and determined the resulting ANE voltage using the reported ANE coefficient [see the Supplemental material B [25]]. As a result, the contributions from the SD-USMR were estimated to be 72% and 118% of the experimentally obtained V_{BG} value for samples E and B, respectively. Using these values, we calculated θ_{SH} for Ta and Pt to be -0.042±0.006 and 0.026±0.006 from Eq. (3), respectively [see also the Supplemental material D [25]]. The calculated value of θ_{SH} for Ta was in the middle between the values estimated from SOT magnetization switching (~–0.12) [42] and spin absorption (~–0.004) [43]. The value of θ_{SH} for Pt was smaller than that estimated from ST-FMR (~0.076) [14]; however, it was consistent with that determined from spin absorption (0.021) [44] and the spin pumping (0.013) [45]. In the estimation of θ_{SH}, the conductivities of Co, Pt, and Ta were electrically measured to be $\sigma_F = 1.01 \times 10^6$ $(\Omega \cdot m)^{-1}$, $\sigma_{Pt} = 1.94 \times 10^6$ $(\Omega \cdot m)^{-1}$, $\sigma_{Ta} = 4.32 \times 10^5$ $(\Omega \cdot m)^{-1}$. The other parameters were obtained from previous works: the spin diffusion lengths of Co, Pt, and Ta, were $L_F = 40$ nm, $L_{Pt} = 14$ nm, and $L_{Ta} = 1.8$ nm [35,46]; the polarization ratio was $p_\sigma - p_N = 0.5$; and the Fermi energy was $\varepsilon_F = 5$ eV [20]. L_F and L_N can also be determined by measuring the t_F and t_N dependences of V_{BG} [21], which allows us to estimate θ_{SH} more precisely.

We emphasize that the V_{BG} signals appeared as background signals not only in the measurements of the LFST-FMR but also those of the ST-FMR, where B_{ext} has a finite angle from the y axis in Fig. 1(a) and the applied f_{MW} is generally high at more than several GHz [see the Supplemental material D [25]]. In the ST-FMR, θ_{SH} is generally estimated from the ratio of the symmetric and antisymmetric components of the FMR signals, where the spin torque generated by the SHE is important. However, the unwanted effects such as the spin pumping, the ANE, phase deviation of the magnetization oscillation, and the non-uniformity of the magnetization, sometimes hinder the precise estimation. Note that θ_{SH} can also be estimated from the background signals induced by the SD-USMR. Because the SD-USMR is induced by the spin-dependent conductivity of the FM and not related to spin torque or magnetization dynamics, we can estimate θ_{SH} from two different perspectives, i.e., spin torque and spin dependent magnetoresistance, by measuring only one FMR spectrum. The unwanted effects are also expected to be different between these two signals. Whereas a precise estimation of the polarization of the electron mobility for the SD-USMR and temperature gradient of the sample for the ANE are not so simple at this stage, it is worth to crosscheck the estimated θ_{SH} values by using both SD-USMR and ST-FMR signals. If we obtain a large θ_{SH} from the amplitude ratio of the symmetric and antisymmetric components of the ST-FMR signal, the BG signal should also increase.

IX. SPIN ORBIT TORQUE MAGNETIZATION SWITCHING

Finally, we detected SOT magnetization switching. In our previous research, we detected SOT magnetization switching using the LFST-FMR [15]. However, because the detection sensitivity depends on the magnitude of the LFST-FMR ($\Delta R_{NM/FM}/\Delta B_{ext}$ at B_{ext} = 0 mT), we expect it to be difficult to use when the FM layer has a low AMR ratio and/or strong coercive field. In this study, we detected SOT magnetization switching using the SD-USMR. When the magnetic easy axis is along the y axis, there is a finite difference in V_{BG} at B_{ext} = 0 mT between the up and down sweeps due to magnetization hysteresis, as shown in Fig. 2. Therefore, we expect that SOT magnetization switching can be detected in the same way as in our previous research [15]. Figure 6(a) shows V_{DC} as a function of B_{ext} at various f_{MW} values for sample F. We confirmed that the SD-USMR was dominant over the LFST-FMR even at low f_{MW} [see the Supplemental material E [25]]. Figure 6(b) shows a schematic of the electric circuit for demonstrating the SOT magnetization switching. First, a strong external magnetic field, B_{SET}, was applied to initialize the magnetization of the Co layer. After removing B_{SET}, we measured the DC voltage representing the initial state of magnetization, V_1, under microwave irradiation. After microwave irradiation was stopped, a pulse current for the SOT magnetization switching was injected into the W channel. Then we measured the DC voltage representing the magnetization direction after the pulse current, V_2, under microwave irradiation. If the magnetization is successfully switched, a non-zero ΔV_{PLS} is observed, where $\Delta V_{PLS} = V_1 - V_2$. Figures 6(c) and 6(d) show the enlarged spectra of V_{DC} (left panels) and ΔV_{PLS} as functions of pulse current density J_{PLS}, i.e., the SOT magnetization switching signal (right panels), where the values of f_{MW} were 0.2 and 13 GHz, respectively. Here, the value of ΔV_{PLS} was set to 0 μV when the magnetization after the injection of J_{PLS} was along $+y$ [15]. Clear hysteresis features were obtained both for f_{MW} = 0.2 and 13 GHz. The magnitude of magnetization switching signal was slightly smaller than that expected from V_{DC}-B_{ext} curves. This is because the magnetization did not completely align along $+y$ or $-y$ direction even though the maximum pulse current of our apparatus was applied. The gradual change in the hysteresis signal is mainly due to the large size of the Co layer, which is consistent with our previous study [15]. The threshold current density was 3×10^7 A/cm^2, which is also consistent with previous research [24]. Here we mention that the SOT magnetization switching can also be detected with an application of DC charge current utilizing the USMR [47] [see the Supplemental material F [25]]. We emphasize that the advantage of using the rectification voltage due to the USMR is the sensitivity. If we use DC charge current, measured voltage increases as increasing the DC charge current, resulting in the increment of the range of the voltmeter and the reduction of the sensitivity. In our method, measured voltage is always around zero no matter how much rf charge current is applied, which enables highly sensitive detection of the SOT magnetization switching.

In demonstrating SOT magnetization switching using the LFST-FMR, one should consider the contribution of the SD-USMR because it modulates the magnitude of magnetization switching signals and might conceal a signal unexpectedly. The contribution ratio of LFST-FMR and SD-USMR can be controlled by adjusting f_{MW}, t_F, and B_{ext}. We emphasize that although the polarities of the LFST-FMR and SD-USMR signals are opposite to each other in the Ta/Co or W/Co systems, it is possible to amplify the sensitivity of SOT switching detection by combining the LFST-FMR and SD-USMR using suitable NM/FM bilayers. For example, the SD-USMR polarity is related to the relative position of the *d*-bands of the host and impurity of the FM layer, and can be changed by controlling the composition. The LFST-FMR polarity can also be changed using the FM layer, which shows negative AMR. The deviation in magnitude from the calculation for the Pt/FM systems we previously reported is also likely due to the SD-USMR contribution.

X. CONCLUSION

In conclusion, we found an additional BG signal superimposed on the LFST-FMR. By measuring the f_{MW}, I_{rf}^0, temperature, and magnetic-field-angle dependences, we concluded the origin of the BG signal to be the SD-USMR. We calculated θ_{SH} for Pt and Ta to be 0.026±0.006 and –0.042±0.006, respectively, using the measured values of V_{BG}. SOT magnetization switching of W/Co was also demonstrated using the hysteresis behavior of V_{BG}. Because the SD-USMR has a weaker relationship with the magnetization dynamics, we demonstrated magnetization switching over a wide range of f_{MW}, even for an FM with a low AMR ratio and/or strong coercive field. Furthermore, by choosing appropriate FM and NM materials, we can use both the LFST-FMR and the SD-USMR, which enable highly efficient detection. Once the parameters in eq. (3); spin diffusion length and the polarization of the electron mobility in the FM; are obtained and the contribution from ANE is experimentally separated, we can estimate θ_{SH} from two different perspectives by only measuring one FMR spectrum because the BG signals appears in the ST-FMR signals. This enables the cross check and more reliable evaluation of θ_{SH}.

Acknowledgements

This work was supported by JSPS (KAKENHI Grant Nos. 16H06330, 19H02197, 20H02607, and 20K22413), JST, and PRESTO (Grant Number JPMJPR20B2).

Data availability

The data that support the findings of this study are available from the corresponding author upon reasonable request.

References

[1] I. Mihai Miron, G. Gaudin, S. Auffret, B. Rodmacq, A. Schuhl, S. Pizzini, J. Vogel, and P. Gambardella, *Current-Driven Spin Torque Induced by the Rashba Effect in a Ferromagnetic Metal Layer*, Nat. Mater. **9**, 230 (2010).

[2] I. M. Miron, K. Garello, G. Gaudin, P.-J. Zermatten, M. V. Costache, S. Auffret, S. Bandiera, B. Rodmacq, A. Schuhl, and P. Gambardella, *Perpendicular Switching of a Single Ferromagnetic Layer Induced by In-Plane Current Injection*, Nature **476**, 189 (2011).

[3] Y. K. Kato, *Observation of the Spin Hall Effect in Semiconductors*, Science **306**, 1910 (2004).

[4] S. O. Valenzuela and M. Tinkham, *Direct Electronic Measurement of the Spin Hall Effect*, Nature **442**, 176 (2006).

[5] S. Dushenko, M. Hokazono, K. Nakamura, Y. Ando, T. Shinjo, and M. Shiraishi, *Tunable Inverse Spin Hall Effect in Nanometer-Thick Platinum Films by Ionic Gating*, Nat. Commun. **9**, 3118 (2018).

[6] Y. Niimi, M. Morota, D. H. Wei, C. Deranlot, M. Basletic, A. Hamzic, A. Fert, and Y. Otani, *Extrinsic Spin Hall Effect Induced by Iridium Impurities in Copper*, Phys. Rev. Lett. **106**, 126601 (2011).

[7] K. Ando, S. Takahashi, J. Ieda, Y. Kajiwara, H. Nakayama, T. Yoshino, K. Harii, Y. Fujikawa, M. Matsuo, S. Maekawa, and E. Saitoh, *Inverse Spin-Hall Effect Induced by Spin Pumping in Metallic System*, J. Appl. Phys. **109**, 103913 (2011).

[8] K. Garello, I. M. Miron, C. O. Avci, F. Freimuth, Y. Mokrousov, S. Blügel, S. Auffret, O. Boulle, G. Gaudin, and P. Gambardella, *Symmetry and Magnitude of Spin-Orbit Torques in Ferromagnetic Heterostructures*, Nat. Nanotechnol. **8**, 587 (2013).

[9] A. R. Mellnik, J. S. Lee, A. Richardella, J. L. Grab, P. J. Mintun, M. H. Fischer, A. Vaezi, A. Manchon, E.-A. Kim, N. Samarth, and D. C. Ralph, *Spin-Transfer Torque Generated by a Topological Insulator*, Nature **511**, 449 (2014).

[10] A. Tsukahara, Y. Ando, Y. Kitamura, H. Emoto, E. Shikoh, M. P. Delmo, T. Shinjo, and M. Shiraishi, *Self-Induced Inverse Spin Hall Effect in Permalloy at Room Temperature*, Phys. Rev. B **89**, 235317 (2014).

[11] J. Jiang, F. Tang, X. C. Pan, H. M. Liu, X. H. Niu, Y. X. Wang, D. F. Xu, H. F. Yang, B. P. Xie, F. Q. Song, P. Dudin, T. K. Kim, M. Hoesch, P. K. Das, I. Vobornik, X. G. Wan, and D. L. Feng, *Signature of Strong Spin-Orbital Coupling in the Large Nonsaturating Magnetoresistance Material WTe2*, Phys. Rev. Lett. **115**, 166601 (2015).

[12] C.-F. Pai, M. Mann, A. J. Tan, and G. S. D. Beach, *Determination of Spin Torque Efficiencies in Heterostructures with Perpendicular Magnetic Anisotropy*, Phys. Rev. B **93**, 144409 (2016).

[13] H. Emoto, Y. Ando, G. Eguchi, R. Ohshima, E. Shikoh, Y. Fuseya, T. Shinjo, and M. Shiraishi, *Transport and Spin Conversion of Multicarriers in Semimetal Bismuth*, Phys. Rev. B **93**, 174428 (2016).

[14] L. Liu, T. Moriyama, D. C. Ralph, and R. A. Buhrman, *Spin-Torque Ferromagnetic Resonance Induced by*

the Spin Hall Effect, Phys. Rev. Lett. **106**, 036601 (2011).

[15] M. Aoki, E. Shigematsu, M. Matsushima, R. Ohshima, S. Honda, T. Shinjo, M. Shiraishi, and Y. Ando, *In-Plane Spin-Orbit Torque Magnetization Switching and Its Detection Using the Spin Rectification Effect at Subgigahertz Frequencies*, Phys. Rev. B **102**, 174442 (2020).

[16] X. F. Zhu, M. Harder, J. Tayler, A. Wirthmann, B. Zhang, W. Lu, Y. S. Gui, and C.-M. Hu, *Nonresonant Spin Rectification in the Absence of an External Applied Magnetic Field*, Phys. Rev. B **83**, 140402 (2011).

[17] M. Aoki, E. Shigematsu, M. Matsushima, R. Ohshima, S. Honda, T. Shinjo, M. Shiraishi, and Y. Ando, *Enhancement of Low-Frequency Spin-Orbit-Torque Ferromagnetic Resonance Signals by Frequency Tuning Observed in Pt/Py, Pt/Co, and Pt/Fe Bilayers*, AIP Adv. **11**, 025206 (2021).

[18] C. O. Avci, K. Garello, A. Ghosh, M. Gabureac, S. F. Alvarado, and P. Gambardella, *Unidirectional Spin Hall Magnetoresistance in Ferromagnet/Normal Metal Bilayers*, Nat. Phys. **11**, 570 (2015).

[19] K. Yasuda, A. Tsukazaki, R. Yoshimi, K. S. Takahashi, M. Kawasaki, and Y. Tokura, *Large Unidirectional Magnetoresistance in a Magnetic Topological Insulator*, Phys. Rev. Lett. **117**, 127202 (2016).

[20] S. S. L. Zhang and G. Vignale, *Theory of Unidirectional Spin Hall Magnetoresistance in Heavy-Metal/Ferromagnetic-Metal Bilayers*, Phys. Rev. B **94**, 140411 (2016).

[21] Y. Yin, D.-S. Han, M. C. H. de Jong, R. Lavrijsen, R. A. Duine, H. J. M. Swagten, and B. Koopmans, *Thickness Dependence of Unidirectional Spin-Hall Magnetoresistance in Metallic Bilayers*, Appl. Phys. Lett. **111**, 232405 (2017).

[22] C. O. Avci, J. Mendil, G. S. D. Beach, and P. Gambardella, *Origins of the Unidirectional Spin Hall Magnetoresistance in Metallic Bilayers*, Phys. Rev. Lett. **121**, 87207 (2018).

[23] I. V. Borisenko, V. E. Demidov, S. Urazhdin, A. B. Rinkevich, and S. O. Demokritov, *Relation between Unidirectional Spin Hall Magnetoresistance and Spin Current-Driven Magnon Generation*, Appl. Phys. Lett. **113**, 062403 (2018).

[24] C.-F. Pai, L. Liu, Y. Li, H. W. Tseng, D. C. Ralph, and R. A. Buhrman, *Spin Transfer Torque Devices Utilizing the Giant Spin Hall Effect of Tungsten*, Appl. Phys. Lett. **101**, 122404 (2012).

[25] See Supplemental Material at [*link*] for more details on the contribution from the field-like spin orbit torque, calculation of the ANE voltage, coexistence of the BG signal and the ST-FMR, estimation of the SHA with various frequencies, BG signal of the W/Co device, and the measurement of the USMR using DC charge current.

[26] W. Nernst, *Ueber Das Auftreten Electromotorischer Kräfte in Metallplatten, Welche von Einem Wärmestrome Durchflossen Werden Und Sich Im Magnetischen Felde Befinden*, Ann. Phys. **265**, 343 (1886).

[27] J. Weischenberg, F. Freimuth, S. Blügel, and Y. Mokrousov, *Scattering-Independent Anomalous Nernst Effect in Ferromagnets*, Phys. Rev. B **87**, 060406 (2013).

[28] A. Slachter, F. L. Bakker, J.-P. Adam, and B. J. van Wees, *Thermally Driven Spin Injection from a Ferromagnet into a Non-Magnetic Metal*, Nat. Phys. **6**, 879 (2010).

[29] M. Erekhinsky, F. Casanova, I. K. Schuller, and A. Sharoni, *Spin-Dependent Seebeck Effect in Non-Local Spin Valve Devices*, Appl. Phys. Lett. **100**, 212401 (2012).

[30] N. Yamashita, Y. Ando, H. Koike, S. Miwa, Y. Suzuki, and M. Shiraishi, *Thermally Generated Spin Signals in a Nondegenerate Silicon Spin Valve*, Phys. Rev. Appl. **9**, 054002 (2018).

[31] C. O. Avci, K. Garello, M. Gabureac, A. Ghosh, A. Fuhrer, S. F. Alvarado, and P. Gambardella, *Interplay of Spin-Orbit Torque and Thermoelectric Effects in Ferromagnet/Normal-Metal Bilayers*, Phys. Rev. B **90**, 224427 (2014).

[32] S. Y. Huang, W. G. Wang, S. F. Lee, J. Kwo, and C. L. Chien, *Intrinsic Spin-Dependent Thermal Transport*, Phys. Rev. Lett. **107**, 216604 (2011).

[33] M. Schmid, S. Srichandan, D. Meier, T. Kuschel, J.-M. Schmalhorst, M. Vogel, G. Reiss, C. Strunk, and C. H. Back, *Transverse Spin Seebeck Effect versus Anomalous and Planar Nernst Effects in Permalloy Thin Films*, Phys. Rev. Lett. **111**, 187201 (2013).

[34] K.-D. Lee, D.-J. Kim, H. Yeon Lee, S.-H. Kim, J.-H. Lee, K.-M. Lee, J.-R. Jeong, K.-S. Lee, H.-S. Song, J.-W. Sohn, S.-C. Shin, and B.-G. Park, *Thermoelectric Signal Enhancement by Reconciling the Spin Seebeck and Anomalous Nernst Effects in Ferromagnet/Non-Magnet Multilayers*, Sci. Rep. **5**, 10249 (2015).

[35] J. Bass and W. P. Pratt, *Spin-Diffusion Lengths in Metals and Alloys, and Spin-Flipping at Metal/Metal Interfaces: An Experimentalist's Critical Review*, J. Phys. Condens. Matter **19**, 183201 (2007).

[36] K. Ueda, T. Koyama, R. Hiramatsu, D. Chiba, S. Fukami, H. Tanigawa, T. Suzuki, N. Ohshima, N. Ishiwata, Y. Nakatani, K. Kobayashi, and T. Ono, *Temperature Dependence of Carrier Spin Polarization Determined from Current-Induced Domain Wall Motion in a Co/Ni Nanowire*, Appl. Phys. Lett. **100**, 202407 (2012).

[37] Q. Hao and G. Xiao, *Giant Spin Hall Effect and Magnetotransport in a Ta/CoFeB/MgO Layered Structure: A Temperature Dependence Study*, Phys. Rev. B **91**, 224413 (2015).

[38] K.-J. Kim, T. Li, S. Kim, T. Moriyama, T. Koyama, D. Chiba, K.-J. Lee, H.-W. Lee, and T. Ono, *Possible Contribution of High-Energy Magnons to Unidirectional Magnetoresistance in Metallic Bilayers*, Appl. Phys. Express **12**, 063001 (2019).

[39] Y. Lv, J. Kally, D. Zhang, J. S. Lee, M. Jamali, N. Samarth, and J.-P. Wang, *Unidirectional Spin-Hall and Rashba−Edelstein Magnetoresistance in Topological Insulator-Ferromagnet Layer Heterostructures*, Nat. Commun. **9**, 111 (2018).

[40] A. Boehnke, M. Walter, N. Roschewsky, T. Eggebrecht, V. Drewello, K. Rott, M. Münzenberg, A. Thomas, and G. Reiss, *Time-Resolved Measurement of the Tunnel Magneto-Seebeck Effect in a Single Magnetic Tunnel Junction*, Rev. Sci. Instrum. **84**, (2013).

[41] K. D. Lee, D. J. Kim, H. Yeon Lee, S. H. Kim, J. H. Lee, K. M. Lee, J. R. Jeong, K. S. Lee, H. S. Song, J. W. Sohn, S. C. Shin, and B. G. Park, *Thermoelectric Signal Enhancement by Reconciling the Spin Seebeck and Anomalous Nernst Effects in Ferromagnet/Non-Magnet Multilayers*, Sci. Rep. **5**, 1 (2015).

[42] H. W. Tseng, C.-F. Pai, R. a. Buhrman, Y. Li, L. Liu, and D. C. Ralph, *Spin-Torque Switching with the Giant Spin Hall Effect of Tantalum*, Science **336**, 555 (2012).

[43] M. Morota, Y. Niimi, K. Ohnishi, D. H. Wei, T. Tanaka, H. Kontani, T. Kimura, and Y. Otani, *Indication of Intrinsic Spin Hall Effect in 4d and 5d Transition Metals*, Phys. Rev. B **83**, 174405 (2011).

[44] J.-C. Rojas-Sánchez, N. Reyren, P. Laczkowski, W. Savero, J.-P. Attané, C. Deranlot, M. Jamet, J.-M. George, L. Vila, and H. Jaffrès, *Spin Pumping and Inverse Spin Hall Effect in Platinum: The Essential Role of Spin-Memory Loss at Metallic Interfaces*, Phys. Rev. Lett. **112**, 106602 (2014).

[45] O. Mosendz, V. Vlaminck, J. E. Pearson, F. Y. Fradin, G. E. W. Bauer, S. D. Bader, and A. Hoffmann, *Detection and Quantification of Inverse Spin Hall Effect from Spin Pumping in Permalloy/Normal Metal Bilayers*, Phys. Rev. B **82**, 214403 (2010).

[46] C. Hahn, G. de Loubens, O. Klein, M. Viret, V. V. Naletov, and J. Ben Youssef, *Comparative Measurements of Inverse Spin Hall Effects and Magnetoresistance in YIG/Pt and YIG/Ta*, Phys. Rev. B **87**, 174417 (2013).

[47] Y.-T. Liu, T.-Y. Chen, T.-H. Lo, T.-Y. Tsai, S.-Y. Yang, Y.-J. Chang, J.-H. Wei, and C.-F. Pai, *Determination of Spin-Orbit-Torque Efficiencies in Heterostructures with In-Plane Magnetic Anisotropy*, Phys. Rev. Appl. **13**, 044032 (2020).

FIGURE CAPTIONS

FIG. 1. (a) Schematic of the device structure and the electrical circuit used in this study. (b, e) $R_{NM/FM}$, (c, f) $-\frac{\Delta R_{NM/FM}}{\Delta B_{ext}}$, and (c, g) V_{DC} as a function of B_{ext} along the y axis for samples A and C, respectively. V_{DC} was measured under microwave irradiation with f_{MW} = 0.2 GHz and microwave power P_{MW} = 5 dBm (I_{rf}^0 = 4.5 mA for sample A and 5.2 mA for sample C).

FIG. 2. (a) V_{DC} as a function of B_{ext} under various microwave frequencies, f_{MW}, and (b) enlarged V_{DC}– B_{ext} curves from −40 to +40 mT (meshed area) for sample C. P_{MW} was 5 dBm with I_{rf}^0 ranging from 4.3 mA at f_{MW} = 13 GHz to 5.2 mA at f_{MW} = 0.2 GHz. (c) V_{DC} as a function of B_{ext} at various f_{MW} values, and (d) enlarged plot for sample D. P_{MW} was 10 dBm, with I_{rf}^0 ranging from 8 mA at f_{MW} = 13 GHz to 10 mA at f_{MW} = 0.2 GHz.

FIG. 3. (a) $V_{BG}/{I_{rf}^0}^2$ as a function of f_{MW} at P_{MW} = 5 dBm with I_{rf}^0 ranging from 4.3 mA at f_{MW} = 13 GHz to 5.2 mA at f_{MW} = 0.2 GHz, and (b) V_{BG} as a function of I_{rf}^0 at f_{MW} = 0.2 GHz for sample C. (c) V_{BG} as a function of temperature for sample E. Under the applied voltage for microwave generation, V_{MW} and f_{MW} were 2 V (I_{rf}^0 = 13 mA) and 0.1 GHz, respectively. Temperature dependence of DC voltage due to the SF-USMR, where the voltage at 300 K is normalized to the same value of V_{BG} at 300 K for sample E.

FIG. 4. (a)−(c) Schematics of the measurement for the magnetic-field-angle dependence of V_{BG}. (d) V_{BG} as a function of α, β, and γ for sample E. V_{MW} and f_{MW} were 2 V (I_{rf}^0 = 13 mA) and 0.1 GHz, respectively.

FIG. 5. Numerically calculated B_{ext} dependence of V_{DC} generated by the SD-USMR for (a) sample A and (b) sample C. The y component of the magnetization was estimated from the anisotropic magnetoresistance (AMR) signal in the $R_{NM/FM}$-B_{ext} curve shown in Figs. 1(c) and 1(d). Difference between experimentally obtained V_{DC}-B_{ext} curves (Figs. 1(d) and 1(g)) and the calculated V_{DC}-B_{ext} curves due to the SD-USMR (Figs. 5(a) and 5(c)) for (c) sample A and (d) sample C.

FIG. 6. (a) V_{DC} as a function of B_{ext} under microwave with various frequencies for W/Co/SiO_2 device with P_{MW} = 5 dBm with I_{rf}^0 ranging from 1.7 mA at f_{MW} = 13 GHz to 2.1 mA at f_{MW} = 0.2 GHz. (b) A schematic of the electrical circuit for demonstration of the magnetization switching. (c,d) Enlarged V_{DC}- B_{ext} curves between −3 to +3 mT (left panels) and ΔV_{PLS} as a function of pulse current density J_{PLS} (right panels) for (c) f_{MW} = 0.2 GHz and (d) 13 GHz.

Table 1. Materials and geometries of samples A−F.

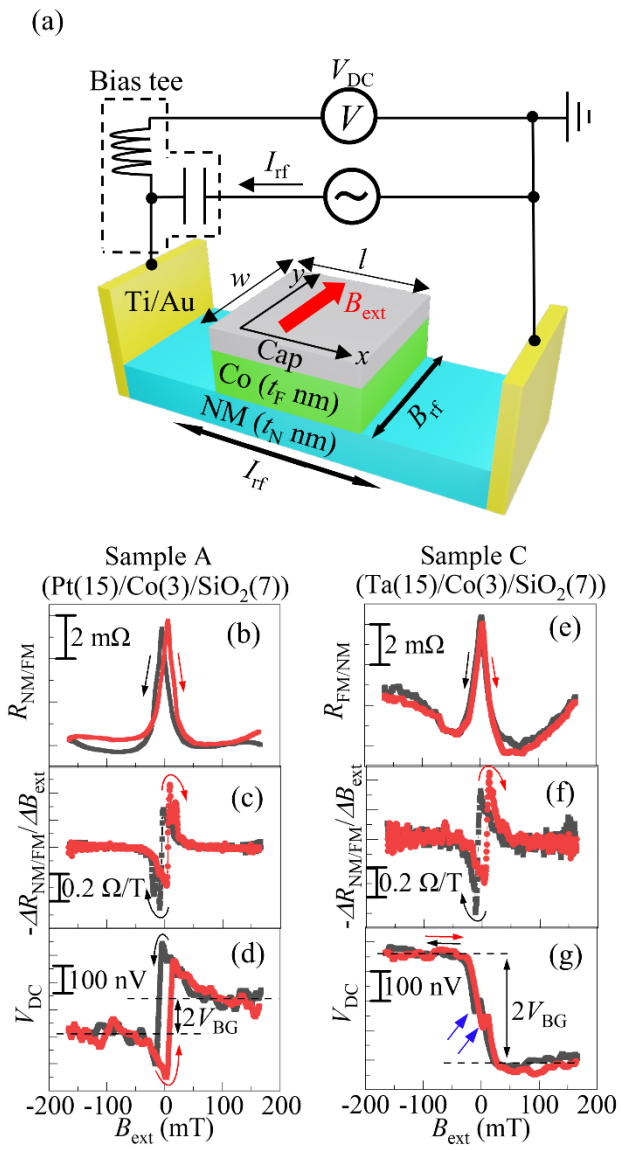

Fig. 1 M. Aoki et al.

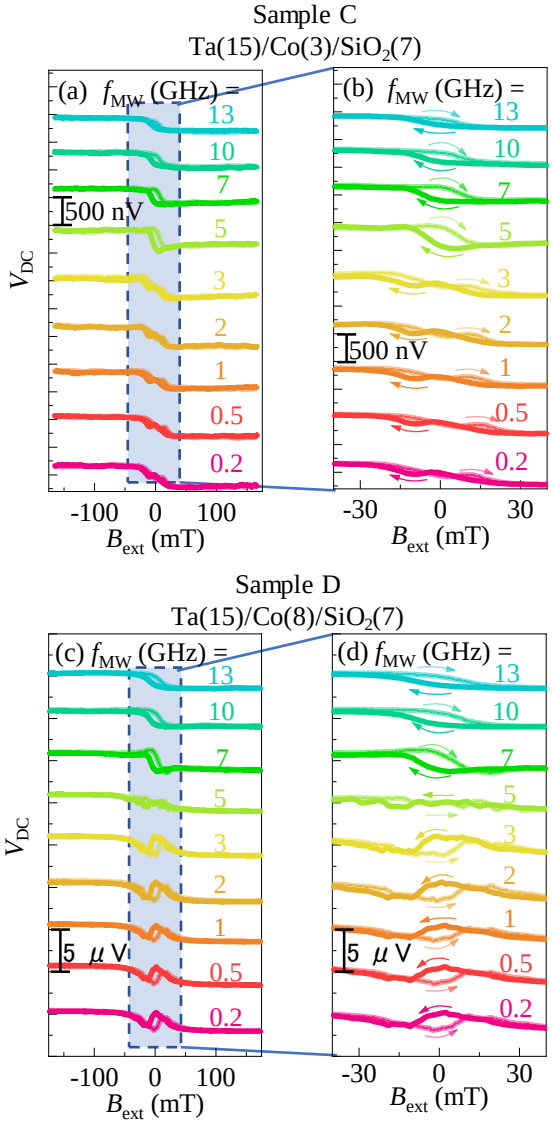

Fig. 2 M. Aoki et al.

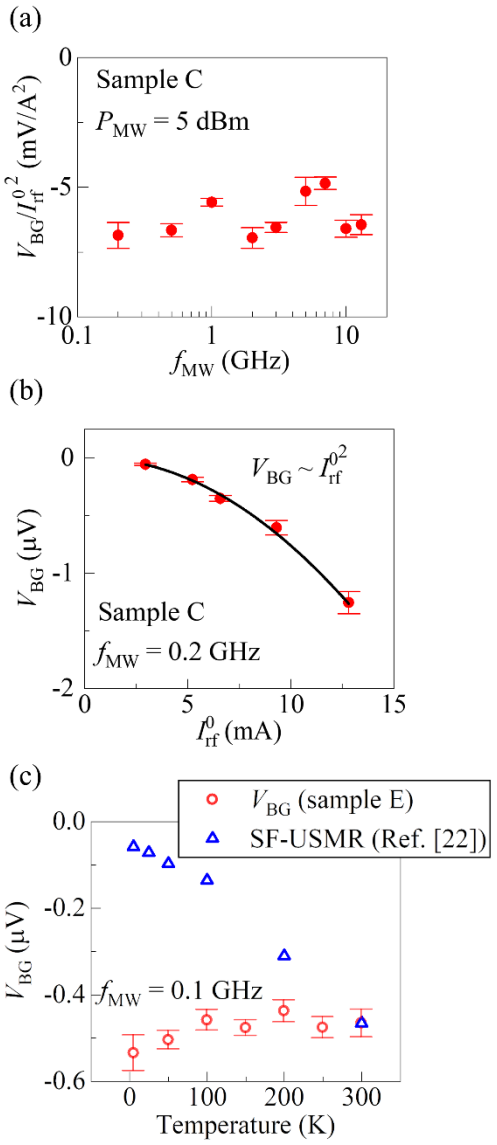

Fig. 3 M. Aoki et al.

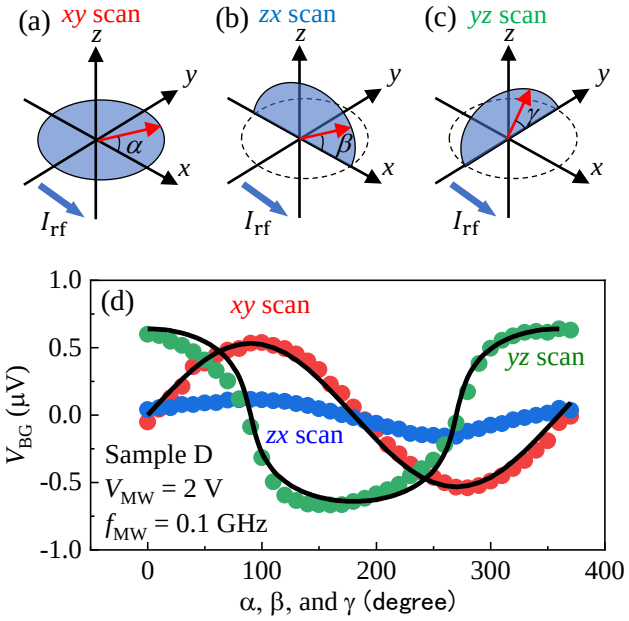

Fig. 4 M. Aoki et al.

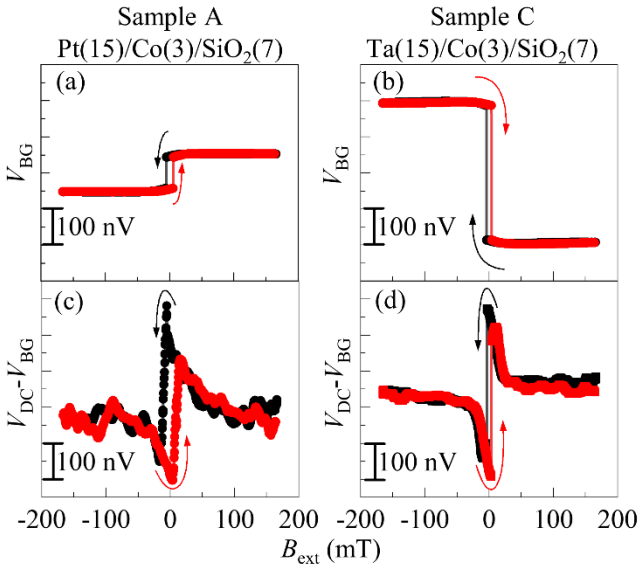

Fig. 5 M. Aoki et al.

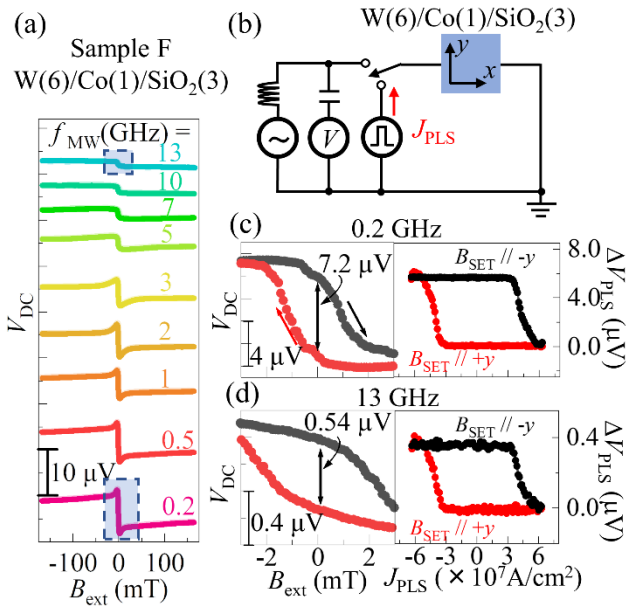

Fig. 6 M. Aoki et al.

Table 1 Aoki et al.

Sample	NM	t_N (nm)	t_F (nm)	t_{cap} (nm)	w (μm)	l (μm)
A	Pt	15	3	7	5	0.8
B	Pt	15	3	7	40	40
C	Ta	15	3	7	5	1
D	Ta	15	8	7	10	1.3
E	Ta	15	3	7	40	40
F	W	6	1	3	5	5